Journal of Materials Processing Tech. 267 (2019) 17–25

Contents lists available at ScienceDirect

Journal of Materials Processing Tech.

journal homepage: www.elsevier.com/locate/jmatprotec

La_2O_3 addition for improving the brazed joints of WC-Co/1Cr13

Y.H. Xiao[a], P.W. Liu[a,c], Z. Wang[a], Y. Wang[b], K.Q. Feng[d], L. Chen[a,*]

[a] Department of Mechanical Engineering, Mississippi State University, MS, 39762, USA
[b] Department of Materials Science and Engineering, The Pennsylvania State University, University Park, PA, 16802, USA
[c] State Key Laboratory of Advanced Design and Manufacturing for Vehicle Body, Hunan University, Changsha, 410082, PR China
[d] College of Manufacturing Science and Engineering, Sichuan University, Chengdu, 610065, PR China

ARTICLE INFO

Associate Editor: C.H. Caceres

Keywords:
Brazed joint
Grain structure
Thermodynamics
Sublattice model
Shear strength

ABSTRACT

The effects of lanthanum oxide (La_2O_3) as an interlayer component on microstructures and mechanical properties of brazed joints of tungsten carbide/cobalt (WC-Co) cemented carbides and the 1Cr13 stainless steel are investigated by an integrated experimental and computational thermodynamics approach. A carbide solid solution phase (CSSP) is experimentally identified adjacent to the detrimental η phase (Co_3W_3C) due to the addition of La_2O_3. Such a CSSP is observed to suppress the formation of η phase. The underlying inhibition mechanism is then explained thermodynamically by comparing the Gibbs free energy of the austenite, CSSP and η phases. The added La_2O_3 is also found to effectively promote the heterogeneous nucleation of the austenite phase, which results in the grain refinement and the uniform distribution of the austenite phase. The shear strength (~340 MPa) of the brazed joints with La_2O_3 addition outperforms the counterparts without La_2O_3.

1. Introduction

The tungsten carbide/cobalt (WC-Co) cemented carbides, mainly composed of WC particles bound by Co phases, are widely intended for cutting, drilling, and mining, due to their excellent wear resistance and high hardness from the compounding properties, as stated by (Upadhyaya, 1998). However, practical applications of such materials are essentially limited by their high cost and poor machinability. To overcome these shortcomings, they are usually joined with structural steel substrates with low cost and good comprehensive performance (Yin et al., 2018).

Many joining technologies have been developed in previous decades, such as injection welding (Chen et al., 2008), friction welding (Dos Santos et al., 2018), microwave welding (Sun et al., 2018), diffusion bonding (Noh et al., 2011) and vacuum brazing (Srinivas et al., 2018). Among them, vacuum brazing is most often used for the cemented carbides/steels joints (Nowacki and Kawiak, 2004), in that (1) it is free of oxidation of the substrates, and (2) the deformation and residual stress induced by the heterogeneous heating can be well mitigated.

Filler materials as the interlayer are crucial to improve the microstructures and welding properties of brazed joints. (Thorsen et al., 1984) have emphasized that the wettability between filler materials and substrates, reflected by the contact angle, plays a crucial role in controlling the occurrence of cracks and porosities during the brazing of cemented carbides. (Zhang et al., 2017) have also pointed out that the wettability determines the brazability of materials by conducting the wetting experiments of Cu/WC-8Co. The results showed that the equilibrium contact angle decreases from 15° to 4° as the temperature increases from 1090 to 1100 °C. (Fu et al., 2016) have discovered the lowest equilibrium contact angle of ~0° at the higher temperature of 1100 °C, due to the strongest interaction between the molten Cu and the WC-Co substrate. Motivated by such a mechanism, the Cu element is widely used as a general component of the interlayer for WC-Co/steel joints, because of the excellent wettability to WC-Co. Also, owing to the favorable match of the thermal expansion coefficients, the residual stress between the Cu alloy and the steel during brazing is almost negligible, which further enables the Cu as one of the outstanding candidates for the filler materials of WC-Co/steel joints.

A brittle eutectic-containing η-phase (Co_3W_3C), however, has been reported in WC-Co/410ss joints when using the Cu as the filler (Chen et al., 2013). The η phase has also been identified by XRD as a network-like pattern, and the mechanical testing shows the η phase is detrimental to mechanical properties of the joints (Jiang et al., 2016). On the other hand, some recent researches have revealed that the formation of the η phase can be well inhibited if the filler material is appropriately composited by the Cu and other materials. For instance, when the Ni-electroplated Cu-Zn alloy is used as the interlayer to get

* Corresponding author.
E-mail address: chen@me.msstate.edu (L. Chen).

https://doi.org/10.1016/j.jmatprotec.2018.11.045
Received 2 August 2018; Received in revised form 26 November 2018; Accepted 29 November 2018
Available online 01 December 2018
0924-0136/

WC-Co/interlayer/3Cr13 joints (Chen et al., 2012), only a small amount of η phase has been discovered. (Barrena et al., 2009) did not report the η phase existence in WC-Co/90MnCrV8 joints when using the 70Ni30Cu alloy as the filler material. Nonetheless, the underlying mechanism governing the suppression of η phase remains rarely explored in the existing studies.

In powder metallurgy, lanthanum oxide (La_2O_3) particles have been treated as heterogeneous nucleation sites, thus leading to grain refinement. (Liu and Yu, 2007) have discovered that the addition of La_2O_3 powder can refine and purify the microstructure and increase the microhardness of the coatings. Meanwhile, the composite coated with 4 wt.% La_2O_3 addition can lead to a 30% enhancement of wear resistance. (WU et al., 2009) have also reported that La_2O_3 addition can promote the heterogeneous nucleation. The La_2O_3 powder exhibits the excellent superiority in cladding and coating for optimizing properties, it, however, has not been employed as a filler component to improve the performance of joints.

In this study, the filler material was made by the Cu-La_2O_3 powdery mixtures. The research on the effects of La_2O_3 addition on the η phase inhibition and mechanical properties of WC-Co/1Cr13 joints were conducted, by an integrated experimental and computational thermodynamics approach. A carbide solid solution phase (CSSP) is experimentally discovered accompanied by a reduction in the quantity of η phase. Thermodynamic approaches are then employed to uncover the inhibition mechanisms of η phase by calculating and comparing the Gibbs free energies of the austenite, CSSP and η phases. Meanwhile, the microstructural morphology of the interlayer is observed with refined grains of the austenite solid solution phase, which contributes to the isotropy of the joints. Finally, the mechanical testing is conducted to demonstrate that a remarkable improvement of the shear strength of the joints can be achieved if an appropriate quantity of La_2O_3 is added to the filler.

2. Materials and experimental methods

The major chemical compositions (wt.%) of the WC-Co cemented carbide used in this study are 90WC and 10Co. The commercially available 1Cr13 stainless steel is utilized with the composition of 0.125C, 13.170Cr, 0.210 Mn, 0.390Si, 0.025S and 0.140Ni (balance 85.94 Fe). WC-Co and 1Cr13 substrates were both machined with the size of 10.0 × 7.0 × 5.0 mm^3 by wire electrical discharge machining. The powdery mixtures of Cu-xLa_2O_3 (x = 0, 0.25, 0.5 and 1.0 wt.%) were purposely obtained by mixing in a stainless-steel ball grinder for 48 h. Subsequently, those mixed powders were pressed into green compacts (7.0 × 5.0 × 0.5 mm^3) as the interlayer, as illustrated in Fig. 1.

Both of the WC-Co and 1Cr13 joined surfaces were ground on the diamond grinding wheel, followed by a well grinding with 240, 360, 400, 800 and 1200 grit sandpapers in sequence. Polishing and ultrasonic cleaning were then performed consecutively before vacuum brazing. Every assembled sample, by sandwiching different mixed

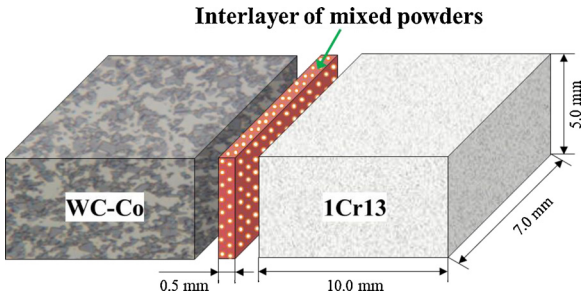

Fig. 1. Schematic of the geometrical and material configurations for a typical brazing dissimilar joint, which includes two substrates i.e., WC-Co and 1Cr13, and one Cu-La_2O_3 powder interlayer.

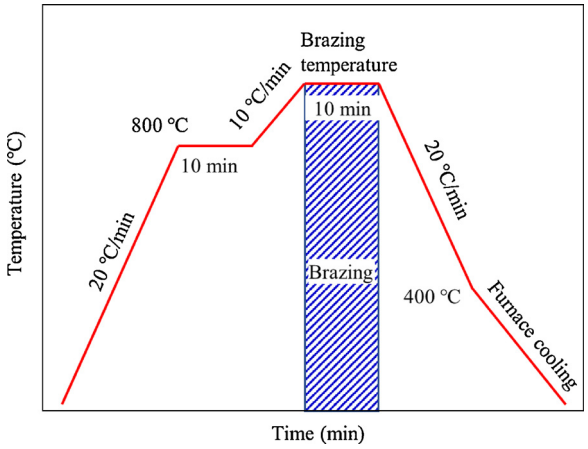

Fig. 2. The thermal brazing curve of WC-Co/interlayer/1Cr13.

green compacts as the interlayer shown in Fig. 1, was put into the vacuum furnace and applied a constant force of approximately 5.0 × 10^3 Pa to help keep the set-up aligned during brazing. Brazing procedures were performed at 1060, 1080 and 1100 °C under a vacuum of 5.0 × 10^{-2} Pa. The thermal brazing curve used in this paper was presented in Fig. 2, with the sintering time set as 10 min as performed in (Chen et al., 2012).

After brazing, the assemblies were cut by a wire cutting machine and the shearing tests were performed by means of a mechanical testing machine to evaluate the mechanical properties of the brazed WC-Co/interlayer/1Cr13 joints. Fig. 3 shows the set-up of shear strength testing. Each value of shear strength is the averaged result from three samples in the same process to guarantee the reproducibility. Also, the brazed samples were cut to get a fresh cross-sectional surface of the joints for the ensuing characterization. The cut samples were also metallographically polished by a standard polishing technique. The microstructures of the WC-Co/interlayer/1Cr13 joints were examined by scanning electron microscopy (SEM) equipped with energy-dispersive X-ray spectrometer (EDX). X-ray diffraction (XRD) was used to detect the fracture surfaces of the joints after the shear strength testing. Electron Probe Micro Analysis (EPMA), equipped with Backscattered electron image (BEI), was used to analyze the microelement (e.g., La) distribution in the interlayer.

3. Computational thermodynamics methods

A combined first-principles/CALPHAD model (Liu, 2009) is used to

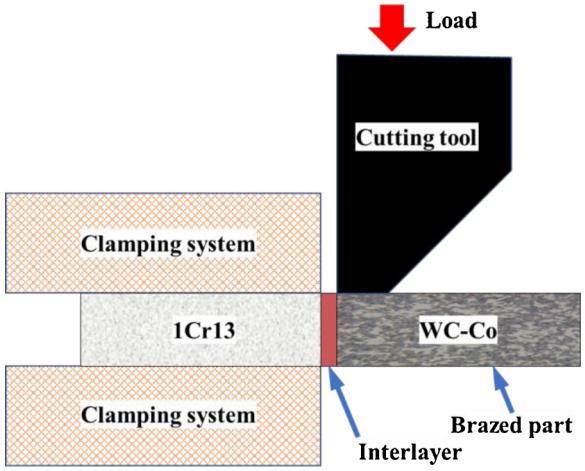

Fig. 3. Schematic of the instrument used to evaluate the shear strength of the brazed joints.

calculate the thermodynamic phase relations including the equilibrium phases and their fractions for each zone in the interlayer. The EDX measured compositions in each zone are used as the input for the calculations. Based on the measured compositions and first-principles energetics, the phase fractions have been calculated using the Dantzig's simplex minimization algorithm (Dantzig et al., 1955). Some energetics reported by the Materials Project (Jain et al., 2013) were utilized. Although these results are based on the 0 K calculations that do not consider solid solution phases, the predicted none-solid solution phases at 0 K, together with the EDX compositions, can still be used as references to determine the region for each phase identified by XRD at ambient temperature. The CALPHAD calculated phases and their fractions can also serve as the basis for estimating the chemical formula of the special phase (CSSP).

Sublattice models, developed by (Hillert and Staffansson, 1970), is capable of describing the solid solution phases. Therefore, they are utilized to compute the Gibbs free energy of each solid solution phase in the interlayer, i.e., the austenite, CSSP and η phases. Then, they can be used to determine the phase formation and their stability against temperature. The comparison of their Gibbs free energies can be used to explain the inhibition mechanisms of η phase.

4. Results and discussion

4.1. Microstructural morphologies

The microstructural morphologies of joints with and without La_2O_3 addition are compared in Fig. 4(a) and (b). As can be seen, there are no defects in both joints brazed at 1080 °C. The morphological changes of the interlayer are mainly manifested in the shape, size, number, and distribution of the austenite solid solution (γ phase), as reported in (Chen et al., 2013). Two major differences of austenite morphologies are clearly identified with La_2O_3 addition, i.e., (1) a certain number of small (~ 60 μm) austenite grains (SAGs) are uniformly distributed in the inner interlayer, and (2) the size of the bulky austenite grain (BAG) adjacent to WC-Co is remarkably reduced from ~500 μm to ~ 100 μm.

The first difference, i.e., the even distribution of SAGs, is attributed to the fact that the La_2O_3 particles can act as the nucleants to form SAGs. The direct evidence is that the SAGs are round or near-round (purple circles) in the inner interlayer of Fig. 4(a), whereas in Fig. 4(b), only a few numbers of elongated austenite grains, as an extension part, connect the BAG. Further, in the manufacturing process of the interlayer, La_2O_3 and Cu powders are homogenously mixed by a longtime planetary ball milling. The EPMA micrograph of the interlayer shown in

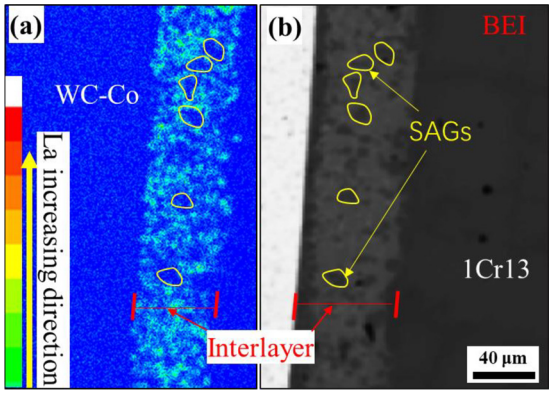

Fig. 5. (a) EPMA micrograph of La element in the interlayer with La_2O_3; (b) BEI image showing small austenite grains (SAGs) marked by yellow cycles that are identified based on the color contrast (For interpretation of the references to colour in this figure legend, the reader is referred to the web version of this article.).

Fig. 5(a) clearly shows the dispersed distribution of La in the interlayer. Hence, the La_2O_3 particles are evenly distributed in the interlayer and act as the nucleation cores to promote heterogenous nucleation, leading to the even distribution of SAGs in the inner interlayer.

Prior to discussing the second difference, i.e., the reduced size of BAG, the mechanisms governing the formation of BAG beside the WC-Co are analyzed. Specifically, the WC-Co surface is basically full of nucleation sites, like interparticle holes and pits, thus the BAG is prone to grow from the WC-Co surface. (Chen et al., 2012) have experimentally proved that the austenite phase tends to nucleate on the micro-rough WC-Co surface instead of the flat 3Cr13 surface. Also, the vast majority of austenite solid solution phase was characterized as columnar crystals along the direction of the WC-Co surface to the 3Cr13 side. Similarly, the BAG in this study presents the columnar crystal structure too, as shown in Fig. 4(b), and some of the branches even reach the length of 500 μm, while there are few branches of BAG in Fig. 4(a). In addition, it should be noted that the coarser microstructure decreases the ductility of the joints (Liu et al., 2018), especially the columnar crystals with strong orientation lead to the anisotropy of properties, which will impair the application of joints (Wu et al., 2002).

The first reason to explain the small BAG after the La_2O_3 addition is the insufficient Fe element that is the main source (Fe) for the BAG formation. In particular, the Fe element has to come across the interlayer to form the BAG. The path of Fe diffusion is partly cut by the SAGs

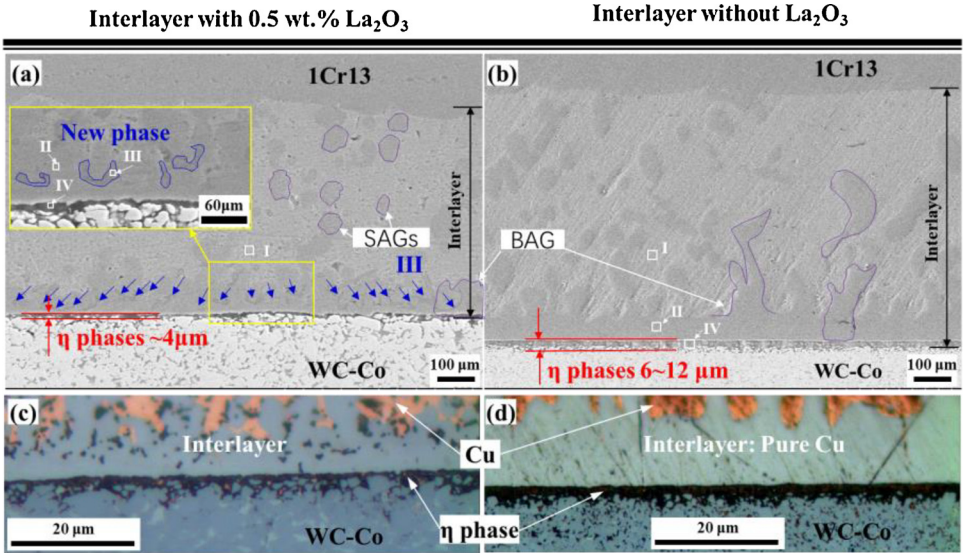

Fig. 4. Etched SEM microstructure and optical microstructure of interlayer Cu-xLa_2O_3/WC-Co at 1080 °C, in which (a) and (c) x = 0.5 wt.%; (b) and (d) x = 0. Many dispersed small austenite grains (SAGs) exist in the interlayer with La_2O_3 addition. The bulky austenite grain (BAG), growing from WC-Co surface, becomes smaller accompanied by the vanishing of crystal arms after adding La_2O_3. The small rectangles (I, II, III and V) are the zones of EDX mapping scan. Each zone is a small part of different phases identified by different contrasts. The remarkably decreased amount of η phase is observed with the appearance of a new phase.

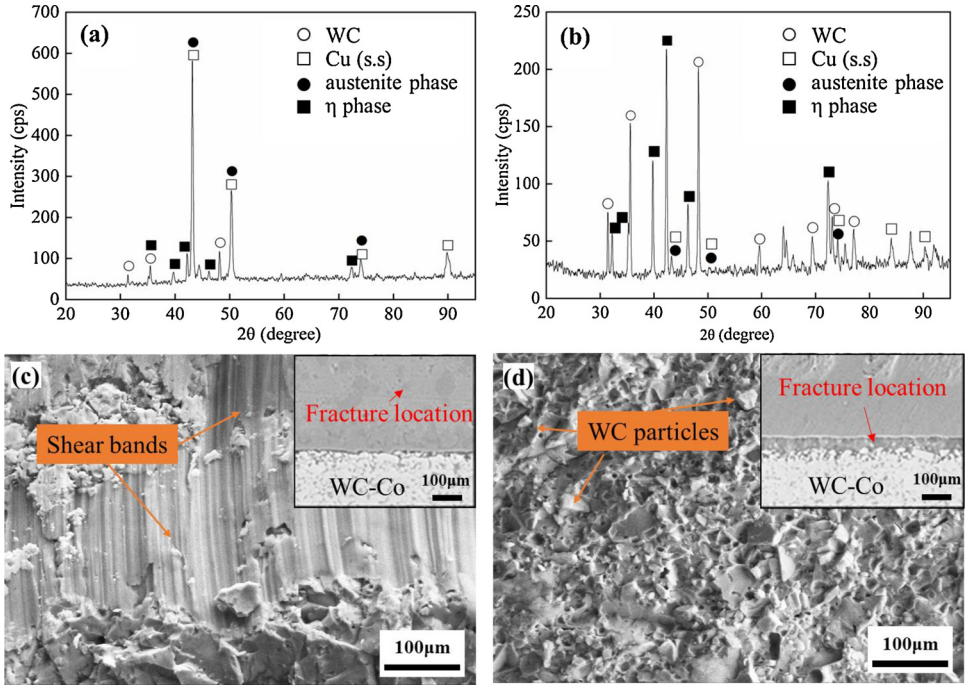

Fig. 6. XRD patterns of fractured surface (WC-Co side) and the corresponding fractographies of WC-Co/Cu-xLa_2O_3/1Cr13 joints, in which (a) and (c) x = 0.5 wt.%; (b) and (d) x = 0. The WC, Cu, austenite and η phases all appears in the joints with or without La_2O_3. The joint with La_2O_3 is observed to exhibit a great number of ductile shear bands, while the fracture surface without La_2O_3 is full of brittle WC particles.

formed in the inner interlayer, thus leading to the deficiency of the Fe element to support the free growth of BAG. Another possible reason is the distribution of La_2O_3 around the austenite phase. In principle, the La_2O_3 could suppress the growth of the austenite phase in that the La element has a large atomic radius, easily acting as a surface-active element distributing beside grain boundaries. It can also be discovered that the SAGs exist in the regions where there is little distribution of La_2O_3, identified by yellow circles, by comparing Fig. 5(a) and (b) (BEI image). Therefore, the La_2O_3 particles are speculated to deliver the pinning effect on the grain boundaries and to retard the growth of SAGs and the BAG.

4.2. Phase analyses

4.2.1. The phases at various regions of the interlayer

Various phases are identified by the X-Ray Diffraction (XRD) on the fracture surfaces (WC-Co side) with and without La_2O_3 addition, as shown in Fig. 6(a) and (b). It can be easily observed that the WC phase, Cu Phase, γ phase and η phase all exist in both cases, but showing different values of diffraction peak intensity. Energy-dispersive X-ray spectrometer (EDX) is then used to measure the compositions for various regions (I, II, III, IV, see Fig. 4) in the interlayer, as tabulated in Tables 1 and 2 for the cases with and without La_2O_3 addition, respectively. The analysis of EDX measured compositions is performed to determine the region for each phase identified by XRD. For example, zone I is mainly composed of Cu element for both of cases (> 60 wt.% as underlined in Tables 1 and 2), thus, it can be regarded to exhibit as the Cu phase. Similarly, the major element of zone II is Fe (> 70 wt.%), thus corresponding to the austenite phase accordingly. Zone IV is

Table 1
EDX results of various zones in the WC–Co/Cu-0.5 wt.% La_2O_3/1Cr13 joint.

Zones	Chemical composition (wt.%)								Main Phase
	C	Cr	Fe	Co	La	Cu	W	O	
I	2.26	1.06	10.92	1.68	13.31	62.27	3.64	4.86	Cu phase
II	1.74	7.12	71.51	8.96	0.28	7.82	1.55	1.00	Austenite
III	8.41	43.03	34.52	2.92	3.35	4.95	2.39	0.43	New phase
IV	17.13	5.88	32.98	6.36	0.00	3.05	27.63	6.97	η phase

Table 2
EDX results of various zones in the WC–Co/Cu/1Cr13 joint.

Zones	Chemical composition (wt.%)								Main Phase
	C	Cr	Fe	Co	La	Cu	W	O	
I	5.32	0.23	4.12	0.50	0.00	87.04	1.28	1.50	Cu phase
II	1.65	8.54	71.49	7.79	0.00	7.90	1.43	1.20	Austenite
IV	11.93	3.34	19.76	11.20	0.00	2.92	26.74	24.12	η phase

essentially made up of four major elements, i.e., Co, W, C, and Fe, which is exactly in accord with the constitutes of η phase (Co_3W_3C or Fe_3W_3C (Dexin and Qingzhang, 2005)). In particular, Zone III is characterized by EDX for the case with La_2O_3 addition, as given in Table 1. It can be seen that Zone III is predominately constituted of C, Cr, Fe, and La, which do not correspond to any phase that has been detected by XRD. Therefore, a new phase, constituted of C, Cr, Fe, and La, was inferred to exist in Zone III, to be discussed in detail in Section 4.4.

Table 3 presents the first-principles/CALPHAD calculated equilibrium phases and their fractions, by using EDX compositions as the input for each zone in the interlayer. The phase that dominates in each zone can be easily verified by the predicted results. Specifically, the Cu phase fraction is found 53% in Zone I, and the Fe phase fraction is 50% in zone II. Both of them are favorably consistent with the analyses of Tables 1 and 2. In Zone IV, four phases, i.e., Co, WC, Fe and $Fe_{11}Co_5$ are found to prevail. Although these calculated phases are merely considered as non-solid solution phases in the model, the constitutions of these phases are again found to be identical to the solid solution η phase. Similarly, some non-solid solution carbides, such as Cr_3C_2, LaC_2, Fe and C are observed in Zone III, which can be used as the basis to estimate the chemical formula of the new phase, to be detailed in Section 4.4.1.

4.2.2. The reduction of the η phase

In this section, the detrimental η phase is comprehensively characterized and interpreted for two cases with and without La_2O_3 addition. By comparing the optical microstructure images of the WC-Co/interlayer shown in Fig. 4(c) and (d), the amount of η phase, identified by the black area etched by Murakami reagent (ASM, 2004), is found to

Table 3
First principles/CALPHAD calculated equilibrium phases and the phase fractions, using the EDX compositions (see Table 1) of each zone as the input.

Zones	Phase fraction (%)										
	C	Cr_3C_2	WC	CO_2	$LaCO_5$	$Fe_{11}Co_5$	Cu	Fe	LaC_2	$LaCu_5$	La_2O_3
I	4.08	1.85	2.16	5.26	20.92	4.98	53.49	7.25	–	–	–
II	0.81	11.95	0.88	4.51	0.42	25.47	6.44	49.52	–	–	–
III	5.21	59.36	1.12	–	–	6.82	–	21.91	0.93	2.72	1.93
IV	34.22	6.56	10.47	22.76	–	12.03	1.06	12.30	–	–	–

decline significantly after adding La_2O_3. Meanwhile, the gap caused by the etched η phase and pointed by red arrows in Fig. 4(b) without La_2O_3, is larger than that in Fig. 4(a) with La_2O_3. Specifically, the thickness of the η phase layer is reduced by three times to below 4.0 μm with La_2O_3 addition. Besides, the XRD results in Fig. 6(a) and (b) show the amount of η phase and WC phase decreases remarkably, accompanying with an increase of Cu phase after adding La_2O_3, according to the diffraction peak intensity of the same phase. Hence, it can be reasonably inferred that the addition of La_2O_3 can effectively inhibit the formation of the η phase, to be discussed in detail in Section 4.4.2.

Another strong evidence to support the phase features listed above is the characteristics of the fracture surfaces for two cases as shown in Fig. 6(c) and (d) respectively. Specifically, without La_2O_3 addition, the typical brittle fracture surface is observed with the WC particles. Such a brittle fracture is mainly attributed to the substantial amount of brittle η phase that results from by the carbon loss of WC. In contrast, with adding La_2O_3, the fracture surface exhibits a great number of shear bands (see Fig. 6(c)), which are the typical ductile fracture characteristics. Such a brittle to ductile fracture transition indicates that a large amount of Cu phase with good ductility, instead of the brittle η phase, is involved in the case with La_2O_3 addition.

4.3. Mechanical characterization

Fig. 7 shows the shear strength of WC-Co/interlayer/1Cr13 joints as a function of the proportion of La_2O_3 at various brazing temperatures T_b = 1060, 1080 and 1100 °C. The brazing time is set to be 10 min for all the cases to guarantee the sufficient diffusion of elements (Chen et al., 2012).

As can be seen, when the brazing temperature T_b is 1080 and 1100 °C, the shear strength firstly increases linearly with the La_2O_3 content followed by significant decrease when the La_2O_3 proportion exceeds 0.5 wt.%. As elaborated above, the La_2O_3 particles, as a role of the nucleants, lead to the refined BAG as well as the dispersed SAGs with a small size. Also, the La_2O_3 favorably suppresses the formation of brittle η phase. Such two mechanisms thus contribute to the increased shear strength with the La_2O_3 addition. However, once the La_2O_3 is excessively added, the shear strength is found to be conversely reduced. The deterioration is possibly pertaining to the fact that the excessive La_2O_3 can act as the impurities rather than the nucleants. Such impurities in principle reduce the wettability and contaminate the interlayer, thus resulting in a sharp deterioration in the weak bonding of the interfaces, namely WC-Co/interlayer and interlayer/1Cr13.

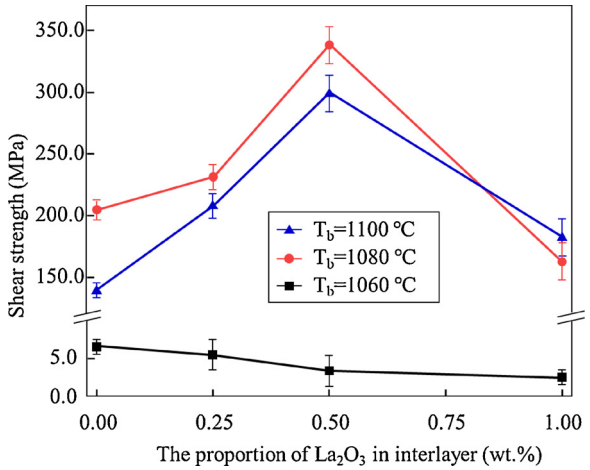

Fig. 7. The effect of the proportion of La_2O_3 on the shear strength of the WC–Co/interlayer/1Cr13 joints at various brazing temperatures.

It can also be seen that the shear strength increases remarkably from 1060 to 1080 °C, followed by a slight decrease at 1100 °C. The increased shear strength from 1060 to 1080 °C is possibly attributed to: (1) the strong diffusion of various elements, (2) the improved wettability and (3) the Cu liquid phase, produced at 1080 °C due to the high surface energy contribution from the powdery interlayer (Sekuli, 2013), can pad the welding seam better, and avoid the defects according to Fig. 4(a) and (b), at an elevated T_b, even in 10 min, compared with the solid Cu phase (Geng et al., 2012). Nonetheless, an excessively increased T_b to 1100 °C is observed to unfavorably weaken the mechanical properties of the joints. One potential reason is that at an excessively increased T_b, the strong diffusion of Fe and C elements results in the coarse austenite phase and the increased amount of brittle η phase. Another possible reason is the partly loss of Cu filler. Specifically, the Cu phase at 1100 °C is almost melted in the form of liquid that shows strong mobility, thus probably flowing away from the interlayer. Overall, the highest shear strength of 340 MPa is obtained at 1080 °C with Cu-0.5 wt.% La_2O_3 interlayer, which is characterized with a well-balanced size, number and morphology of austenite and η phases. It is worth noting that 340 MPa in the shear strength is higher than the 320 MPa that has been demonstrated with the outstanding mechanical performance in (Chiu et al., 2008), where the pure Cu foil was used as the interlayer.

4.4. Discussion

4.4.1. The new phase

Two more evidences, besides the extensive analyses of Tables 1–3, have been identified to confirm the existence of a new phase in the interlayer due to the La_2O_3 addition. The first evidence comes from the SEM image that captures a hooklike particle pointed by zone III, which appears only in the case with La_2O_3 addition, as shown in Fig. 4(a). Secondly, the appearance of the new phase can be identified by comparing the EDX composition profiles of elements for two cases with and without La_2O_3 addition, as shown in Fig. 8(a∼d) and (e∼h) respectively. It can be clearly seen that as La_2O_3 is added, the elements Fe, Cr, Cu show an abrupt change (marked with red line), which strongly demonstrate the appearance of the new phase, as indicated by the red arrow in Fig. 8(a).

The chemical formula of the new phase is subsequently speculated based on the EDX compositions. Herein, the hypothesis that the new phase in Zone III is a carbide solid solution phase (CSSP) was made, as it involves a complex mixture of carbides, such as Cr-C, La-C, Fe and C as presented in Table 3. The EDX results also clearly show that the new phase has a high content of C, Fe, Cr and La. Further, the new phase is directly adjacent to the solid solution η phase. Based on these, the chemical formula of the new phase can be inferred to be expressed as

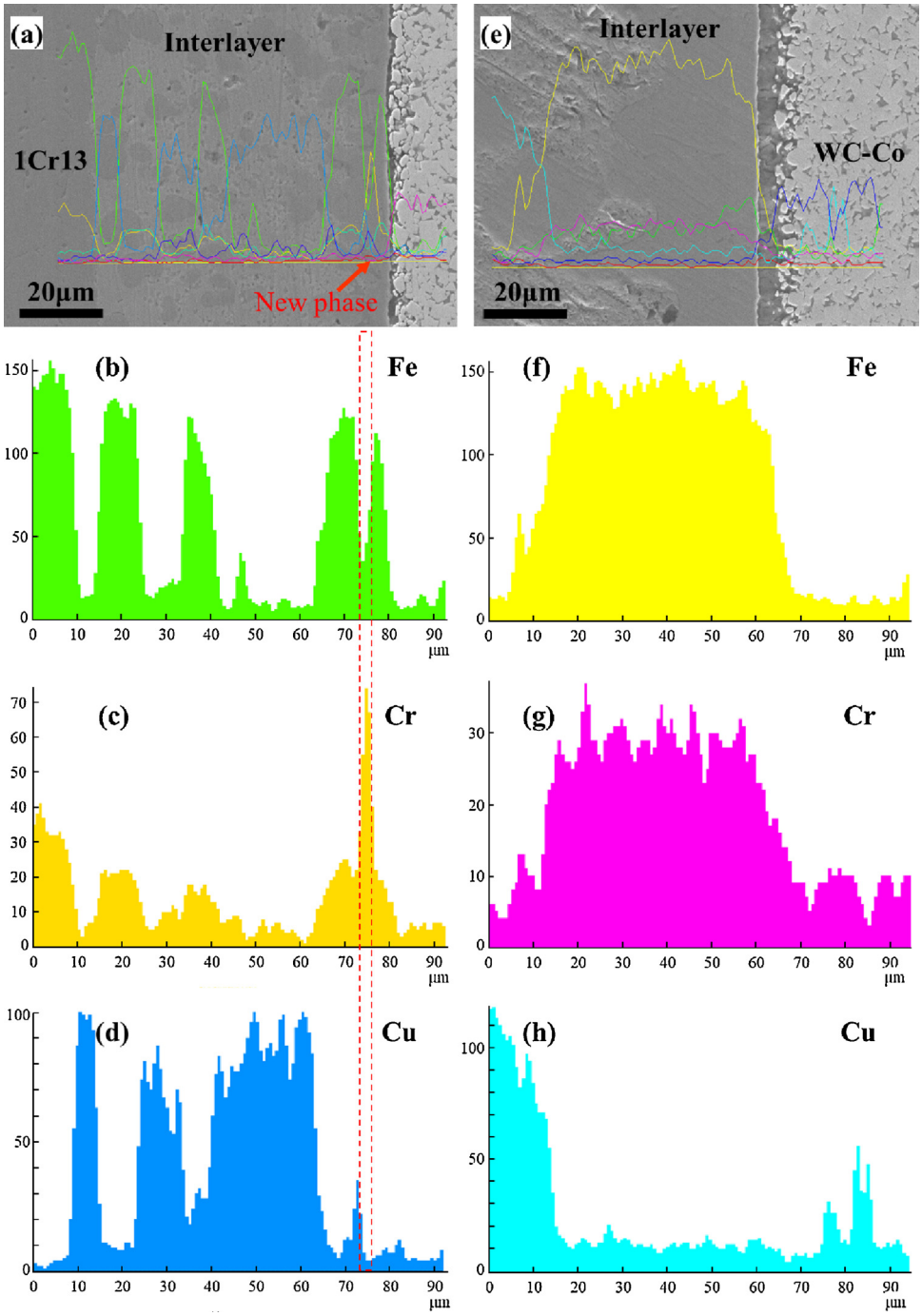

Fig. 8. EDX line scan analysis across the joints (beside WC-Co), in which (a), (b), (c) and (d): x = 0.5 wt.%; (e), (f), (g) and (h): x = 0. The saltation of Fe, Cr and Cu elements (marked by red line) indicates the appearance of a new phase after adding La_2O_3 (For interpretation of the references to colour in this figure legend, the reader is referred to the web version of this article.).

$(Fe, Cr, La)_yC_x$, which well explains the high content of C, Fe, Cr and La. The chemical formula can be further used for evaluating the Gibbs free energy of the CSSP phase to interpret its inhibition effect on the formation of the η phase, as detailed below.

4.4.2. Inhibition mechanisms for the η phase

- Carbon concentration

The first potential mechanism to inhibit the η phase formation is related to the C concentration. No η phase forms when filling metals contain above 0.8 wt.% C, as experimentally proved by (Zhao et al., 2011). In this study, the concentration of C in zone III is far larger than 0.8 wt.%, which, therefore, contributes to a strong habitation mechanism. In principle, the formation of the η phase occurs by decarburization in the WC-Co that is expressed as:

$$3WC + 3Co \rightarrow Co_3W_3\ C + 2C \quad (1)$$

in which, the high concentration of C indicates a large chemical activity of the reaction product, thus acting as a strongly negative driving force to the WC decarburization reaction of WC and the formation of η phase. However, it takes some time to form the new phase CSSP, the η phase is not fully inhibited as shown with the gap in Fig. 4(a).

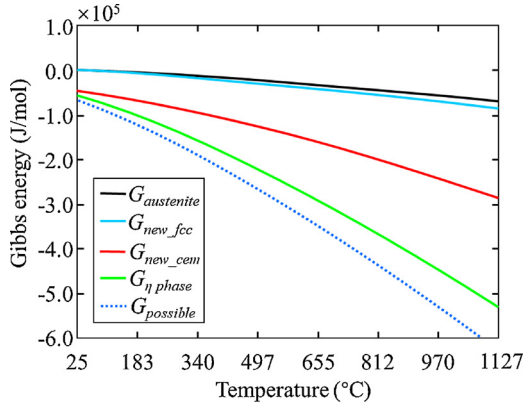

Fig. 9. Gibbs free energy G_m as a function of the temperature T for the three major phases in the interlayer, i.e., the austenite, η and new CSSP phases. The subscripts new_fcc and new_cem indicate, respectively, the face-centered cubic structure and cementite structure for the new CSSP phase. $G_{possible}$ is achieved when all parameters of G_m function are considered.

- Computational thermodynamics analysis

In order to further explain the inhibition mechanisms of η phase, the Gibbs free energy (G_m) of each phase is calculated and compared, using the thermodynamic CALPHAD method, to predict the phase formation and their stability. Three major phases in the interlayer, i.e., the austenite, the new phase CSSP and the η phase (Co_3W_3C), are employed for the purpose of comparison. The detailed calculation based on different sublattice models are presented in Appendix A.

Fig. 9 shows the Gibbs free energy G_m against the temperature T for the three phases in the interlayer. It is obvious that at the brazing temperature of 1080 ℃, all the G_m values of three phases are much less than zero, which implies that three phases all stably form at this brazing temperature from a thermodynamics point of view. Moreover, although the G_m increases as the cooling proceeds, i.e., the temperature, T decreases, the G_m values for all of three phases are still below zero, indicating their existence at room temperature (25 ℃). By comparing these phases, it can be readily deduced that the η phase is most likely to form thermodynamically during the brazing, followed by the CSSP with cementite structures, the CSSP with FCC structures, and the austenite. This can well explain why there is the stable CSSP phase existing in the austenite with the La_2O_3 addition.

It is also worth noting that with two assumed sublattice structures above, the G_m of the CSSP phase fails to be lower than that of the η phase. Therefore, its inhibition effect on the formation of the η phase becomes relatively weak. $G_{possible}$ curve in Fig. 9 can also be attained when further study is carried out to assure all the parameters. If so, $G_{possible}$ will support that the priority of the CSSP formation is higher than that of the η phase.

The inhibition mechanism can be further investigated by the chemical potential or activity of C in various phases, which essentially control the diffusion trend. However, the analyses of chemical activity rely on a stronger database with more thermodynamics and kinetics parameters. Another concern is the chemical formula and the crystal structure of the CSSP phase. In this study, they are only estimated based on the EDX compositions. Advanced characterization techniques, such as in-situ TEM or micro-area XRD, have been demonstrated to effective tools to detect the crystal structure of a little new phase. We are still working to introduce TEM to characterize more information about the CSSP phase, which will be reported in another paper.

5. Conclusions

- The dispersed La_2O_3 particles, as a role of the nucleants, lead to the refined BAG as well as the evenly distributed SAGs with a small size, which can avoid the anisotropy of mechanical properties.
- A carbide solid solution phase (CSSP) is experimentally identified adjacent to the detrimental η phase (Co_3W_3C) due to the addition of La_2O_3. It is predominately constituted of Fe, Cr, C and La.
- Based on the experimental analyses of the SEM, XRD and EDX, the amount of the η phase decreases remarkably due to the appearance of the CSSP phase.
- The high C concentration in the CSSP indicates a large chemical activity of the WC decarburization reaction product, thus acting as a strongly negative driving force to the formation of the η phase.
- Since the Gibbs energies of three phases, i.e., the austenite, the CSSP, and the η phase, are much smaller than zero, they can stably exist during brazing. Considering the easy formation of CSSP and the relatively small Gibbs energy, it can block the growth of η phase.
- The shear strength of WC-Co/interlayer/1Cr13 joints is the synthesized effects of microstructural morphology and the amount of the η phase, increasing firstly and then decreasing with the increase of the La_2O_3 content or brazing temperature. The maximum shear strength value is 340 MPa at 1080 ℃ for 10 min when the La_2O_3 content in the interlayer is 0.5 wt.%.

Acknowledgments

This work is financially supported by the program of ORAU Ralph E. Powe Junior Faculty Enhancement Award and NSF CMMI 1662854. The authors thank the Analytical & Testing Center of Sichuan University for the testing of the samples. P.W. Liu is grateful for the financial support by Hunan Provincial Innovation project of graduate student (CX2017B081) and the China Scholarship Council. The authors are grateful for Y. Z. Ji at Penn State for useful discussions on thermodynamic analyses.

Appendix A. The calculation of G_m by sublattice models

Two-sublattice model is used for the austenite phase. For one unit formula of an interstitial solution $Fe_1(C, Va)_1$, the sublattice model yields.

$$G_m^{fcc} = y_C^{II}\,{}^{o}G_{Fe:C}^{fcc} + y_{Va}^{II}\,{}^{o}G_{Fe:Va}^{fcc} + RT\left(y_C^{II}\ln y_C^{II} + y_{Va}^{II}\ln y_{Va}^{II}\right) + y_C^{II}y_{Va}^{II}L_{Fe:C,Va}^{fcc}, \quad \text{(S1)}$$

where y_C^{II} and y_{Va}^{II} are the site fractions of component C and vacancy respectively, on the interstitial sublattice (II). y_C^{II} is set as a constant value of 0.02155 when 2.11% is considered as the maximum solid solubility of C in austenite, so that G_m^{fcc} is exclusively a function of temperature T. ${}^{o}G_{Fe:Va}^{fcc}$ is the Gibbs free energy of pure Fe in a hypothetical nonmagnetic state. ${}^{o}G_{Fe:C}^{fcc}$ is the Gibbs free energy of hypothetical nonmagnetic state where all the interstitial sites are filled with the C element. $L_{Fe:C,Va}^{fcc}$ is the free energy due to interaction, in which the comma separates components that interact in the same sublattice. All the values are given according to the enthalpy of selected reference states for the elements at 298.5 K, i.e., the stable element reference (SER). All the parameters are referenced from (Andersson, (1988)

Four-sublattice model $Co_2W_2(Co, W)_2C$ is used to depict the M_6C (Co_3W_3C) phase, developed by (Guillermet, 1989) in Co-W-C system and the expression for the Gibbs free energy of M_6C yields.

$$G_m^{M_6C} = y_{Co}^{III}\,{}^{o}G_{Co:W:Co:C}^{M_6C} + y_W^{III}\,{}^{o}G_{Co:W:W:C}^{M_6C} + 2RT\left(y_{Co}^{III}\ln y_{Co}^{III} + y_W^{III}\ln y_W^{III}\right) + {}^{E}G_m^{M_6C}, \quad \text{(S2)}$$

The parameters ${}^{o}G^{M_6C}_{Co:W:Co:C}$ and ${}^{o}G^{M_6C}_{Co:W:W:C}$ are the Gibbs energy of the carbide with Co or W in the third sublattice. Their values are expressed with respect to the selected reference states for the elements, in the following expressions:

$$G^{M_6C}_{Co:W:Co:C} = 4\,{}^{o}G^{hcp}_{Co:Va} + 2\,{}^{o}G^{bcc}_{W:Va} + {}^{o}G^{graph}_{C} + \Delta G^{M_6C}_{Co:W:Co:C}, \tag{S3}$$

$$G^{M_6C}_{Co:W:W:C} = 2\,{}^{o}G^{hcp}_{Co:Va} + 4\,{}^{o}G^{bcc}_{W:Va} + {}^{o}G^{graph}_{C} + \Delta G^{M_6C}_{Co:W:W:C},\ G^{fcc}_{m} \tag{S4}$$

where $\Delta^{\circ} G^{M_6C}_{Co:W:Co:C}$ and $\Delta^{\circ} G^{M_6C}_{Co:W:W:C}$ are two correction parameters, which are treated as linearly dependent on temperature and evaluated by computerized optimization of the experimental data. ${}^{o}G^{hcp}_{Co:Va}$ is the Gibbs free energy of pure Co in a hypothetical nonmagnetic state with the structure hcp. $G^{bcc}_{W:Va}$ is the Gibbs free energy of pure W in a hypothetical nonmagnetic state with the structure bcc. y^{III}_{Co} and y^{III}_{W} are 0.5. However, the excess energy term ${}^{E}G^{M_6C}_{m}$ is equal to zero.

Further, for the new phase CSSP, two assumptions of sublattice are made to estimate the Gibbs free energy of the CSSP. Because the Fe, Cr, La and C system has not been studied, but is similar to the Co-Fe-Ni-W-C system investigated by (Fernández Guillermet, 1989), the assumed two sublattice models are referenced from the Co-Fe-Ni-W-C system. The first one is the two-sublattice model $(Fe, Cr, La)_1(C, Va)_1$ (fcc) and the can be expressed as follows

$$\begin{aligned} G^{fcc}_{m} = {} & y^{I}_{Fe}y^{II}_{C}\,{}^{o}G^{fcc}_{Fe:C} + y^{I}_{Cr}y^{II}_{C}\,{}^{o}G^{fcc}_{Cr:C} + y^{I}_{La}y^{II}_{C}\,{}^{o}G^{fcc}_{La:C} + y^{I}_{Fe}y^{II}_{Va}\,{}^{o}G^{fcc}_{Fe:Va} + y^{I}_{Cr}y^{II}_{Va}\cdot{}^{o}G^{fcc}_{Cr:Va} + y^{I}_{La}y^{II}_{Va}\,{}^{o}G^{fcc}_{La:Va} + RT\cdot(y^{I}_{Fe}\ln y^{I}_{Fe} + y^{I}_{Cr}\ln y^{I}_{Cr} + y^{I}_{La}\ln y^{I}_{La}) + RT \\ & \cdot(y^{II}_{C}\ln y^{II}_{C} + y^{II}_{Va}\ln y^{II}_{Va}) + {}^{E}G^{fcc}_{m} + \Delta G^{mg}_{m} \end{aligned} \tag{S5}$$

where y^{I}_{Fe} y^{I}_{Cr} and y^{I}_{La} are calculated according to the ratio in EDX after the normalization process of the three components. y^{II}_{C} is set to 0.3, to reduce the variables of G_m function. ΔG^{mg}_{m} is the magnetic contribution to the Gibbs energy equal to zero. The term ${}^{E}G^{fcc}_{m}$ in Eq. (5) represents the excess Gibbs energy of the CSSP with fcc. It is expressed as follows

$$\begin{aligned} {}^{E}G^{fcc}_{m} = {} & y^{I}_{Fe}y^{I}_{Cr}\,(y^{II}_{C}L^{fcc}_{Fe,Cr:C} + y^{II}_{Va}L^{fcc}_{Fe,Cr:Va}) + y^{I}_{Fe}y^{I}_{La}\,(y^{II}_{C}L^{fcc}_{Fe,La:C} + y^{II}_{Va}L^{fcc}_{Fe,La:Va}) + y^{I}_{Cr}y^{I}_{La}\,(y^{II}_{C}L^{fcc}_{Cr,La:C} + y^{II}_{Va}L^{fcc}_{Cr,La:Va}) \\ & + y^{II}_{C}y^{II}_{Va}\,(y^{I}_{Fe}L^{fcc}_{Fe:C,Va} + y^{I}_{Cr}L^{fcc}_{Cr:C,Va} + y^{I}_{La}L^{fcc}_{La:C,Va}), \end{aligned} \tag{S6}$$

where $L^{fcc}_{Fe,Cr:C}$, $L^{fcc}_{Fe,Cr:Va}$, $L^{fcc}_{Fe,La:C}$, $L^{fcc}_{Fe,La:Va}$, $L^{fcc}_{Cr,La:C}$, $L^{fcc}_{Cr,La:Va}$, $L^{fcc}_{Fe:C,Va}$, $L^{fcc}_{Cr:C,Va}$ and $L^{fcc}_{La:C,Va}$ are the free energy due to interaction, in which the comma separates components that interact in the same sublattice.

The other is that the new phase is assumed as a two-sublattice model $(Fe, Cr, La)_3C$ (cementite).

$$G^{cem}_{m} = y^{I}_{Fe}\,{}^{o}G^{cem}_{Fe:C} + y^{I}_{Cr}\,{}^{o}G^{cem}_{Cr:C} + y^{I}_{La}\,{}^{o}G^{cem}_{La:C} + 3RT\cdot(y^{I}_{Fe}\ln y^{I}_{Fe} + y^{I}_{Cr}\ln y^{I}_{Cr} + y^{I}_{La}\ln y^{I}_{La}) + {}^{E}G^{M_6C}_{m} + \Delta G^{mg}_{m}, \tag{S7}$$

where ${}^{o}G^{cem}_{Fe:C}$, $G^{cem}_{Cr:C}$ and ${}^{o}G^{cem}_{La:C}$ are the Gibbs free energy of hypothetical nonmagnetic state where all the second sites are filled with the C element in the cementite structure. All the parameters are cited (Fernández Guillermet, 1989) and (Peng et al., 2011). All lacked data are treated as zero.

References

Andersson, J.-O., 1988. A thermodynamic evaluation of the Fe-Cr-C system (1988). Metall. Trans. A. 19, 627–636. https://doi.org/10.1007/BF02649276.

ASM, 2004. Metallography: an introduction, metallography and microstructures. International ASM Metals Handbook. https://doi.org/10.1361/asmhba0003771.

Barrena, M.I., de Salazar, J.M.G., Matesanz, L., 2009. Ni-Cu alloy for diffusion bonding cermet/steel in air. Mater. Lett. 63, 2142–2145. https://doi.org/10.1016/j.matlet.2009.06.042.

Chen, H., Feng, K., Wei, S., Xiong, J., Guo, Z., Wang, H., 2012. Microstructure and properties of WC-Co/3Cr13 joints brazed using Ni electroplated interlayer. Int. J. Refract. Met. Hard Mater. 33, 70–74. https://doi.org/10.1016/j.ijrmhm.2012.02.018.

Chen, H., Feng, K., Xiong, J., Guo, Z., 2013. Characterization and stress relaxation of the functionally graded WC-Co/Ni component/stainless steel joint. J. Alloys Compd. 557, 18–22. https://doi.org/10.1016/j.jallcom.2012.12.152.

Chen, L., Li, J., Zhou, H., Li, D., He, Z., Tang, Q., 2008. A study on gas-assisted injection molding filling simulation based on surface model of a contained circle channel part. J. Mater. Process. Technol. 208, 90–98. https://doi.org/10.1016/j.jmatprotec.2007.12.118.

Chiu, L.H., Wang, H.F., Huang, C.P., Hsu, C.T., Chen, T.C., 2008. Effect of brazing temperature on the microstructure and property of vacuum brazed WC-Co and carbon steel joint. Advanced Materials Research Vol 47. Trans Tech.Publ, pp. 682–685. https://doi.org/10.4028/www.scientific.net/AMR.47-50.682.

Dantzig, G.B., Orden, A., Wolfe, P., 1955. The generalized simplex method for minimizing a linear form under linear inequality restraints. Pacific J. Math. 5, 183–195.

Dexin, S.Y.Z.X.Y., Qingzhang, Z.X.W., 2005. microstructure analysis of the TIG interface of YG30 cemented carbide and steel 45. Cem. Carbide. 2, 002.

Dos Santos, J.F., Staron, P., Fischer, T., Robson, J.D., Kostka, A., Colegrove, P., Wang, H., Hilgert, J., Bergmann, L., Hütsch, L.L., Huber, N., Schreyer, A., 2018. Understanding precipitate evolution during friction stir welding of Al-Zn-Mg-Cu alloy through in-situ measurement coupled with simulation. Acta Mater. 148, 163–172. https://doi.org/10.1016/j.actamat.2018.01.020.

Fernández Guillermet, A., 1989. The Co-Fe-Ni-W-C phase diagram: a thermodynamic description and calculated sections for (Co-Fe-Ni) bonded cemented WC tools. Z. Metallkd. 80, 83–94.

Fu, H., Zhang, X., Liu, G., Xu, Z., Pan, T., Qiao, G., 2016. Wetting and interfacial behaviors of molten Ag, Cu and Ag-28Cu on WC-8Co cemented carbide. Key Eng. Mater. 697. https://doi.org/10.4028/www.scientific.net/KEM.697.555.

Geng, D., Wu, B., Guo, Y., Huang, L., Xue, Y., Chen, J., Yu, G., Jiang, L., Hu, W., Liu, Y., 2012. Uniform hexagonal graphene flakes and films grown on liquid copper surface. Proc. Natl. Acad. Sci. https://doi.org/10.1073/pnas.1200339109.

Guillermet, A.F., 1989. Thermodynamic properties of the Co-W-C system. Metall. Trans. A. 20, 935–956. https://doi.org/10.1007/BF02651660.

Hillert, M., Staffansson, L.-I., 1970. The regular solution model for stoichiometric phases and ionic melts. Acta Chem. Scand. 24, 3618–3626. https://doi.org/10.3891/acta.chem.scand.24-3618.

Jain, A., Ong, S.P., Hautier, G., Chen, W., Richards, W.D., Dacek, S., Cholia, S., Gunter, D., Skinner, D., Ceder, G., 2013. Commentary: the materials project: a materials genome approach to accelerating materials innovation. Appl. Mater. 1, 011002. https://doi.org/10.1063/1.4812323.

Jiang, C., Chen, H., Wang, Q., Li, Y., 2016. Effect of brazing temperature and holding time on joint properties of induction brazed WC-Co/carbon steel using Ag-based alloy. J. Mater. Process. Technol. 229, 562–569. https://doi.org/10.1016/j.jmatprotec.2015.09.044.

Liu, P.W., Ji, Y.Z., Wang, Z., Qiu, C.L., Antonysamy, A.A., Chen, L.Q., Cui, X.Y., Chen, L., 2018. Investigation on evolution mechanisms of site-specific grain structures during metal additive manufacturing. J. Mater. Process. Technol. 257, 191–202. https://doi.org/10.1016/j.jmatprotec.2018.02.042.

Liu, X.B., Yu, R.L., 2007. Effects of La2O3on microstructure and wear properties of laser clad γ/Cr7C3/TiC composite coatings on TiAl intermatallic alloy. Mater. Chem. Phys. 101, 448–454. https://doi.org/10.1016/j.matchemphys.2006.08.013.

Liu, Z.K., 2009. First-principles calculations and CALPHAD modeling of thermodynamics. J. Phase Equilibria Diffus. 30, 517. https://doi.org/10.1007/s11669-009-9570-6.

Noh, S., Kasada, R., Kimura, A., 2011. Solid-state diffusion bonding of high-Cr ODS ferritic steel. Acta Mater. 59, 3196–3204. https://doi.org/10.1016/j.actamat.2011.01.059.

Nowacki, J., Kawiak, M., 2004. Deformability of WC-Co sinters and 17-4 PH steel brazed joints. J. Mater. Process. Technol. 157, 584–589. https://doi.org/10.1016/j.jmatprotec.2004.07.118.

Peng, Y., Du, Y., Zhang, L., Sha, C., Liu, S., Zheng, F., Zhao, D., Yuan, X., Chen, L., 2011. Thermodynamic modeling of the C-RE (RE = La, Ce and Pr) systems. Calphad 35, 533–541. https://doi.org/10.1016/j.calphad.2011.09.002.

Sekuli, D.P., 2013. Advances in brazing: science, technology and applications. Adv. Brazing: Sci., Technol. Appl. https://doi.org/10.1533/9780857096500.

Srinivas, V., Singh, A.K., Gopala Krishna, V., Madhusudhan Reddy, G., 2018. Vacuum brazing of dissimilar tubular component of AA2219 and AISI 304 by a low melting Al-18Ag-20Cu-5Si-0.2Zn braze alloy. J. Mater. Process. Technol. 252, 1–12. https://doi.org/10.1016/j.jmatprotec.2017.09.005.

Sun, X., Wu, G., Yu, J., Du, C., 2018. Efficient microwave welding of polypropylene using graphite coating as primers. Mater. Lett. 220, 245–248. https://doi.org/10.1016/j.matlet.2018.03.046.

Thorsen, K., Fordsmand, H., Praestgaard, P.L., Thorsen, K.A., Fordsmand, H., Praestgaard,

P.L., 1984. Explanation of wettability problems when brazing cemented carbides. Weld. J. (Miami) 63, 308.

Upadhyaya, G.S., 1998. Cemented tungsten carbides. Cemented Tungsten Carbides. https://doi.org/10.1016/B978-081551417-6.50002-2.

Wu, A.P., Zou, G.S., Ren, J.L., Zhang, H.J., Wang, G.Q., Liu, X., Xie, M.R., 2002. Microstructures and mechanical properties of Ti–24Al–17Nb (at.%) laser beam welding joints. Intermetallics 10, 647–652. https://doi.org/10.1016/S0966-9795(02)00049-3.

Wu, C., Ma, M., Liu, W., Zhong, M., Zhang, H., Zhang, W., 2009. Laser cladding in-situ carbide particle reinforced Fe-based composite coatings with rare earth oxide addition. J. Rare Earths 27, 997–1002. https://doi.org/10.1016/S1002-0721(08)60377-4.

Yin, G., Xu, P., Gong, H., Cui, H., Lu, F., 2018. Effect of interlayer thickness on the microstructure and strength of WC-Co/Invar/316L steel joints prepared by fibre laser welding. J. Mater. Process. Technol. 255, 319–332. https://doi.org/10.1016/j.jmatprotec.2017.12.030.

Zhang, X.Z., Liu, G.W., Tao, J.N., Shao, H.C., Fu, H., Pan, T.Z., Qiao, G.J., 2017. Vacuum brazing of WC-8Co cemented carbides to carbon steel using pure Cu and Ag-28Cu as filler metal. J. Mater. Eng. Perform. 26, 488–494. https://doi.org/10.1007/s11665-016-2424-6.

Zhao, X.J., Chen, C.H., Sun, Y., Yang, D.X., Tagashira, K., 2011. The effect of carbon content in filling alloys on η phase formation in the interface zone of YG30 and weld bead. Advanced Materials Research Vol 189. Trans Tech Publications, pp. 3309–3312.